Available online at www.sciencedirect.com
ScienceDirect
Ceramics International 35 (2009) 1819–1827
CERAMICS INTERNATIONAL
www.elsevier.com/locate/ceramint

Preparation of stabilized Gd-doped $BaPrO_3$ materials by Zr substitution

A. Magrasó [a,*], X. Solans [b,1], J.T.S. Irvine [c], M. Segarra [a]

[a] DIOPMA Centre, IN2UB, Department of Materials Science and Metallurgical Engineering, University of Barcelona, Martí i Franquès 1, 08028 Barcelona, Spain
[b] Crystallography and Mineralogy Department, Geology Faculty, University of Barcelona, Martí i Franquès 1, 08028 Barcelona, Spain
[c] School of Chemistry, Purdie Building, University of St. Andrews, Fife KY16 9ST, Scotland, UK

Received 14 December 2007; received in revised form 22 September 2008; accepted 4 October 2008
Available online 21 October 2008

Abstract

The synthesis of a Gd-doped $BaPrO_3$–$BaZrO_3$ solid solution has been investigated in an effort to stabilize the $BaPrO_3$ perovskite, a system with poor chemical stability and endurance for humid, CO_2 and reducing conditions. The phases $BaZr_xPr_{1-x}Gd_{0.3}O_{3-\delta}$ ($x = 0$–0.7, $\Delta x = 0.1$) have been prepared by acrylamide combustion synthesis. The solid solution is characterized by X-ray powder diffraction, scanning electron microscope (SEM) and durability against CO_2, moisture and reducing conditions investigated. Crystal structure parameters were obtained from X-ray powder diffraction data and results show its symmetry increases by increasing Zr content. $BaZr_{0.1}Pr_{0.6}Gd_{0.3}O_{3-\delta}$ has a maximum weight increase due to reaction with CO_2 of nearly 13%, while this is reduced below 2% for $BaZr_{0.5}Pr_{0.2}Gd_{0.3}O_{3-\delta}$. The material appears to be unaltered by 5%H_2/Ar for $x \geq 0.5$, and under wet Ar for $x \geq 0.4$, and thus render a higher chemical stability and confirms the stabilizing role of $BaZrO_3$. However, microstructure investigations reveal gadolinium segregation due to the high doping level of the perovskite.

Keywords: A. Powders: chemical preparation; D. Perovskites; $BaZrO_3$; $BaPrO_3$

1. Introduction

Perovskite-type oxide materials (ABO_3) have received significant attention due to their wide range of technological applications, in particular fuel cells, hydrogen sensors, batteries, electrochemical hydrogen pumps, electrochemical micro-reactors, etc. [1–7].

Gd-doped $BaPrO_3$ is an attractive material for fuel cell applications [8–10], but a prolonged exposure to wet or reducing gases (or CO_2) leads to its mechanical disintegration and final decomposition [11–13]. Similarly, $BaCeO_3$ compounds are not stable in CO_2-containing atmosphere below 800 °C [14]. On the other hand, acceptor-doped $BaZrO_3$ present an excellent chemical stability and mechanical strength [15,16].

Thermodynamic stability, or at least long-term kinetic stability, of the material at operation conditions is essential to ensure reliable performance and long service life of the device. Bhide et al. [17] studied the thermodynamic stability of several perovskites ($BaMO_3$, M = Ce, Pr, Zr, Ti, niobates, tantalates and other related perovskites), and found that $BaMO_3$ with M = Ce and Pr decomposed to form $Ba(OH)_2$ and the respective hydroxide in boiling water, while M = Ti, Zr did not.

Some efforts have been devoted towards stabilizing $BaCeO_3$ materials by partially replacing Ce by Zr. Previous reports have proved that the chemical stability of Zr-substituted barium cerates significantly increased in comparison with the unsubstituted material [18,19]. Incorporation of 20% Zr on the tetravalent cation site in Nd-doped barium cerate completely retards the decomposition reaction [18].

The scope of the present work is mainly focused to enhance chemical stability of $BaPrO_3$ by gradually replacing Pr by Zr, as well as evaluating the phase purity and microstructure of the new materials. Since the reducibility of the metal ions follows this order: Pr > Ce ≫ Zr, the increase of Zr content should improve the chemical durability against water, reducing conditions, and CO_2. The new family of compounds, $BaZr_xPr_{1-x-y}Gd_yO_{3-\delta}$, may be significant as possible SOFC materials with enhanced stability compared to the Zr-free parent material.

* Corresponding author.
E-mail address: annamagraso@gmail.com (A. Magrasó).
[1] Passed away on 3 September 2007.

0272-8842/$34.00
doi:10.1016/j.ceramint.2008.10.006

In terms of synthesis procedure, the acrylamide combustion route was chosen, as it is a very convenient wet chemical synthesis method in order to provide ultrafine, highly disagglomerated, nanometric powders, which are of particular interest because of their low-temperature sinterability and compositional homogeneity. This synthesis route has been demonstrated to produce ceramic oxide powders for SOFCs with improved homogeneity and microstructure [20–22].

2. Experimental work

2.1. Synthesis

Fine powders of $BaZr_xPr_{0.7-x}Gd_{0.3}O_{3-\delta}$ ($x = 0$–0.7, $\Delta x = 0.1$) were prepared using the acrylamide combustion synthesis [22]. Stoichiometric quantities of Pr_6O_{11}, Gd_2O_3 and $ZrO(NO_3)_2{\cdot}xH_2O$ (all 99.9% purity, Alfa Aesar, Karlsruhe, Germany), and $BaCO_3$ (99.95%, DIOPMA, Barcelona, Spain) were dissolved in an aqueous solution of nitric acid heated at $T \sim 80$ °C. After the complete dissolution of the oxides and carbonates, tetra-acid EDTA (Quality Chemicals, Esparreguera, Spain) was added to the solution in order to chelate all the cations that would interfere in the polymerization of acrylamide [21]. A 1:1 cation:EDTA ratio was assumed. The pH was then adjusted between 6 and 8 by NH_4OH additions in order to adjust the solution acidity. The next step consisted in the gellification using acrylamide (99% purity, Aldrich) and N,N′-methylenbisacrylamide (99% purity, Aldrich), which acts as crosslinker. We also added a small amount of α-α′-azobutyronitrile (98% purity, Fluka Chemical AG, Buchs, Switzerland) as a thermochemical initiator. Polymerization and, consequently, gel formation, occurs within a few seconds, when the temperature reaches 80 °C, approximately.

This gel was heated up until the mixture was completely dried and burnt, and then submitted to 550 °C for 2 h to decompose most of the organic compounds. The resulting fluffy powders contained in each case a fine mixture of oxides and carbonates which served as a precursor material for the formation of each $BaZr_xPr_{0.7-x}Gd_{0.3}O_{3-\delta}$ composition. The formation and evolution of the phase with temperature was studied by subsequent thermal treatments between 900 and 1500 °C, for 10 h. Alumina crucibles were used for thermal treatments until 1200 °C, whereas platinum crucibles were used for $T > 1300$ °C, since reaction between alumina and our material occurs around those temperatures.

2.2. Structural characterization

Phase identification was carried out in a Phillips PW 1710 or Siemens D-500 X-ray diffractometer. The operating parameters involved in XRD data used are as follows: Cu Kα radiation (with $k_{\alpha 2}$ contribution), 15–90° as the 2θ scanning range, 0.2°/min and 0.02 as the scanning speed and step, respectively. The parameters for indexing and cell-parameter calculations were collected at a scanning mode of a step of 0.01 and a scanning rate of 0.1 °C/min. The lattice parameters were obtained using the FullProf and WinPlotr suite softwares [23].

2.3. Microstructural characterization

Particle size and morphology of the powders were examined by FE-SEM (Hitachi S-4100) device operating at 30 kV. All preparations were covered with a thin film of carbon to avoid charging problems and to obtain better image definition. Also, the crystallite size was determined from the FWHM given by the refinement routine and using the Scherrer equation.

2.4. Stability studies

TGA analyses were performed in wet 5% H_2–Ar and wet Ar to assess chemical stability under reducing conditions and water over the temperature range of 25–900 °C. Also 100% CO_2 TGA analysis were collected to check the stability versus the formation of $BaCO_3$ until 1000 °C. The heating rate was 5 °C/min in all cases. X-ray diffraction was performed after the experiment to analyze the resulting products.

3. Results and discussion

3.1. Phase formation and structure

$BaZr_xPr_{0.7-x}Gd_{0.3}O_{3-\delta}$ ($x = 0$, 0.1, 0.2, 0.3, 0.4, 0.5, 0.6 and 0.7) nanopowders were successfully prepared by the acrylamide combustion route after one single thermal treatment directly from the precursor at the desired temperature. In Fig. 1a, a series of XRD patterns for the $BaZr_{0.4}Pr_{0.3}Gd_{0.3}O_{3-\delta}$ composition are displayed. A minimal amount of precursors, identified as $BaCO_3$ (pdf: 45-1471) and Gd_2O_3 (pdf: 42-1465), remains at 900 and 1000 °C, but no appreciable impurity peaks appear over 1100 °C, the minimum calcination temperature. Moreover, the XRD peaks at 1100 °C look very broad compared to those calcined at 1400 °C (as emphasized in Fig. 2), which can be attributed a very small particle size, in the submicronic range.

The materials have the simple cubic (or almost-cubic) perovskite structure, and form a single phase material in all the compositional range (Fig. 3). All the strong peaks are reflections corresponding to the primitive cubic lattice of an ideal perovskite-type structure (as labelled in Fig. 3). These strong peaks gradually shift the peak positions to higher angles with the increase of x (Zr), showing solid solution phases.

The minimum calcination temperature in order to obtain the pure phase varies from 1000 °C (for $x = 0$–0.1), 1100 °C ($x = 0.2$–0.4) up to 1200 °C (for $x = 0.5$–0.7), thus higher calcination temperature is needed for higher Zr content. This is an expected behaviour, since ZrO_2 is more refractory and less reactive with BaO compared to PrO_x. The XRD patterns for $BaZr_{0.2}Pr_{0.5}Gd_{0.3}O_{3-\delta}$ and $BaZr_{0.5}Pr_{0.2}Gd_{0.3}O_{3-\delta}$ are displayed in Fig. 1b and c, respectively, as examples of different calcination temperature as the amount of zirconium varies. The perovskite phase is formed at 900 °C in all cases, although there is still some precursor precipitation at that temperature.

Refinement of the lattice constants were accomplished, and indexing of the PXRD patterns was attempted to the space groups *Pnma* (orthorhombic; pdf: 70-1430) [24] and *Pm*-3*m*

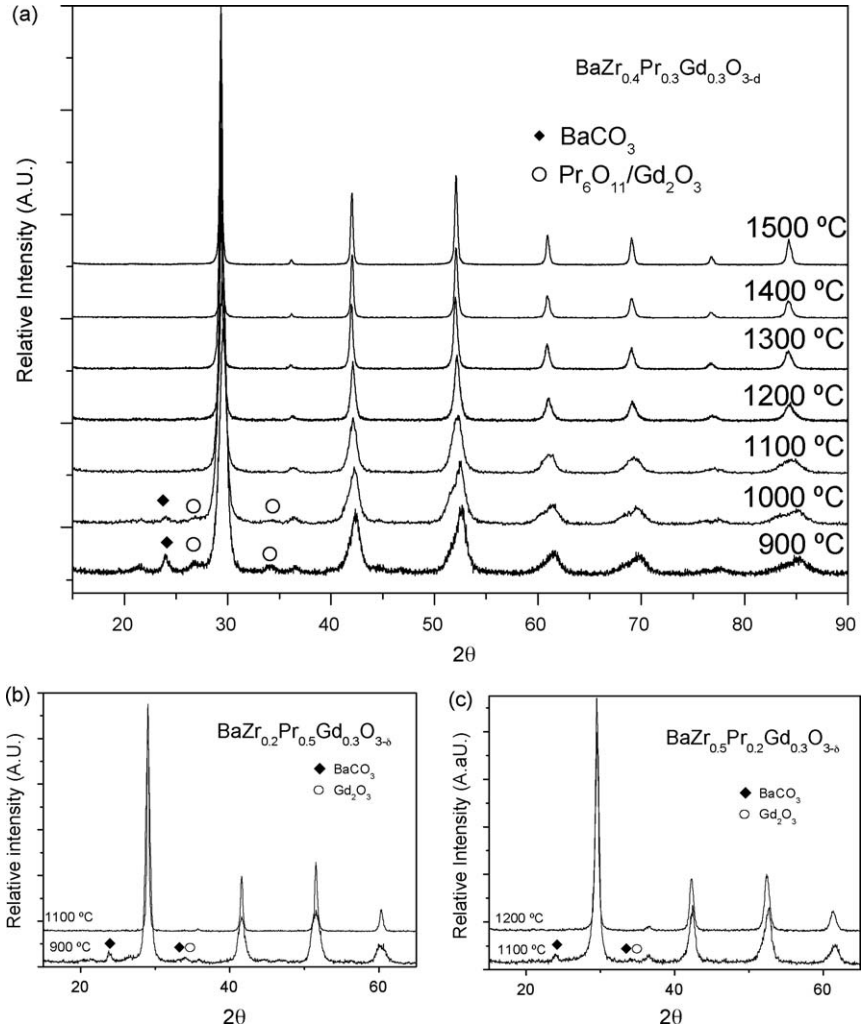

Fig. 1. X-ray diffraction patterns of: (a) gel derived $BaZr_{0.4}Pr_{0.3}Gd_{0.3}O_{3-\delta}$ treated at different temperatures for 10 h, and selected patterns for (b) $BaZr_{0.2}Pr_{0.5}Gd_{0.3}O_{3-\delta}$ calcined at 900 and 1100 °C and (c) for $BaZr_{0.5}Pr_{0.2}Gd_{0.3}O_{3-\delta}$ calcined at 1100 and 1200 °C.

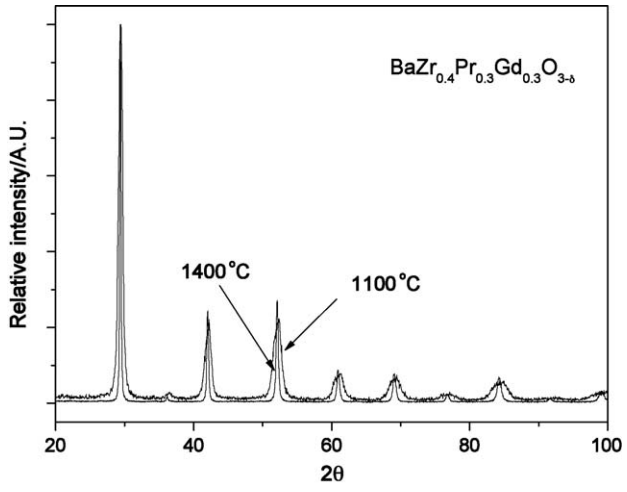

Fig. 2. Comparative XRD patterns for the $BaZr_{0.4}Pr_{0.3}Gd_{0.3}O_{3-\delta}$ powder calcinated at 1100 and 1400 °C. There is a noticeable peak width difference due to the existence of nanometric material at the lowest temperature.

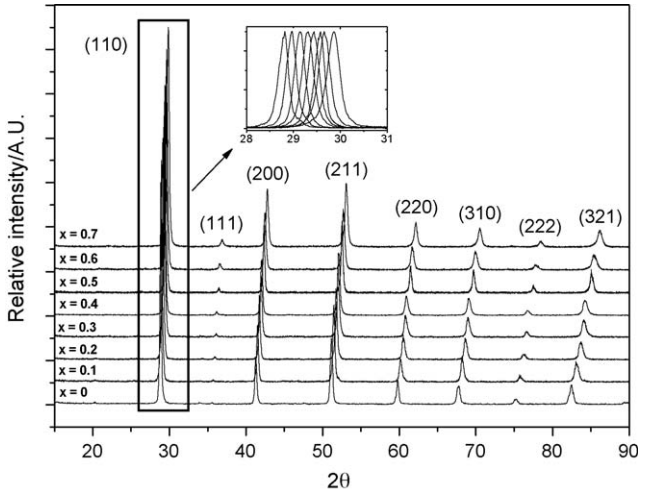

Fig. 3. X-ray diffractogram sequence for the $BaZr_xPr_{0.7-x}Gd_{0.3}O_{3-\delta}$ ($0 \geq x \geq 0.7$) of well crystallized samples ($T = 1400$ °C). Indexing corresponds to the *Pm*-3*m* symmetry.

Table 1
Results of lattice parameters refinement by X-ray powder diffractometry for $BaZr_xPr_{0.7-x}Gd_{0.3}O_{3-\delta}$ ($0 \geq x \geq 0.7$). The number in parentheses is the uncertainty in the last digit, as given by the lattice parameter refinement routine.

	Phase[a]	a (Å)	b (Å)	c (Å)
$BaPrO_3$ [9]	O	6.181 (1)	6.214 (1)	8.722 (1)
$BaPrO_3$	O	6.176 (2)	6.207 (2)	8.720 (2)
$BaPr_{0.7}Gd_{0.3}O_{3-\delta}$	O	6.179 (2)	6.216 (2)	8.735 (2)
$BaZr_{0.1}Pr_{0.6}Gd_{0.3}O_{3-\delta}$	O	6.138 (2)	6.167 (2)	8.756 (2)
$BaZr_{0.2}Pr_{0.5}Gd_{0.3}O_{3-\delta}$	O	6.105 (2)	6.135 (2)	8.679 (2)
$BaZr_{0.3}Pr_{0.4}Gd_{0.3}O_{3-\delta}$	O	6.067 (2)	6.117 (2)	8.657 (2)
$BaZr_{0.4}Pr_{0.3}Gd_{0.3}O_{3-\delta}$	C	4.294 (2)	–	–
$BaZr_{0.5}Pr_{0.2}Gd_{0.3}O_{3-\delta}$	C	4.276 (2)	–	–
$BaZr_{0.6}Pr_{0.1}Gd_{0.3}O_{3-\delta}$	C	4.248 (2)	–	–
$BaZr_{0.7}Gd_{0.3}O_{3-\delta}$	C	4.218 (2)	–	–
$BaPr_{0.9}Gd_{0.1}O_{3-\delta}$	O	6.177 (2)	6.204 (2)	8.724 (2)
$BaZr_{0.3}Pr_{0.6}Gd_{0.1}O_{3-\delta}$	O	6.087 (2)	6.124 (2)	8.613 (2)
$BaZr_{0.6}Pr_{0.3}Gd_{0.1}O_{3-\delta}$	C	4.263 (2)	–	–
$BaZrO_3$ [10]	C	4.1930	–	–

[a] C/O denote cubic/orthorhombic structures, respectively.

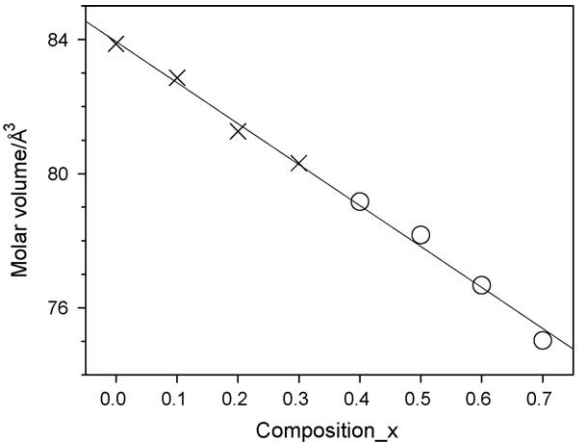

Fig. 4. Variation of the molar volume versus the Zr content in $BaZr_xPr_{0.7-x}Gd_{0.3}O_{3-\delta}$ calculated using XRD patterns calcined at 1400 °C. It follows Vegard's law of ideal solid solutions.

(cubic; pdf: 06-0399) [25]. The lattice parameters determined in this study are summarized in Table 1. The phases are cubic when the content of Zr is high, orthorhombically distorted when the content in Pr is high, due to lattice distortion as the B-site becomes too big for the ideal *Pm*3-*m* aristotype. In those cases, it is possible to appreciate several very low intensity peaks, e.g. next to the (1 1 1) reflection (for the *Pm*-3*m* space group) at $2\theta \sim 34^\circ$. This denotes a non-cubic reflection that one can observe, at least, until $x = 0.3$. Then, we assume that for $x > 0.4$ the perovskite is cubic. We may note, however, that the distortion from the cubic ideal perovskite is quite small, even for the Pr end member, so a higher resolution technique is needed to confirm a more precise space group. For that purpose, the use of synchrotron radiation to assess structural elucidation of related materials is currently underway. Nonetheless, it is clear that the extent of the orthorhombic distortion decreases with increasing the Zr content, as expected from the symmetry reported for the end members. All peaks shift towards higher 2θ, and the relative intensities of some of the peaks change gradually as a function of composition. The variation of the molar cell volume due to the substitution of Pr(IV) for Zr(IV) follows a linear relationship (see Fig. 4), which is in accord with Vegard's law of ideal solid solutions, as the ionic radius of Zr^{4+} ($R = 0.72$ Å) is smaller than that of Pr^{4+} ($R = 0.85$ Å) [26].

3.2. Powder morphology

Surface morphology and microstructure of the powder at each temperature were observed by FE-SEM. The variation of the microstructure of $BaZr_{0.4}Pr_{0.3}Gd_{0.3}O_{3-\delta}$ powders with temperature can be appreciated from Fig. 5. The powders fired at 1100 °C show a highly porous morphology of the aggregates, and particle sintering occurs with the increase of temperature, particularly over 1200 °C. Nanosized quasi-spherical particles, with a size of 80–120 nm can be observed for the powders calcined at 1100 °C from micrographs in selected areas taken at higher magnification (Fig. 5b). Primary aggregates of those particles can be identified, thus forming aggregates bigger than 250 nm. Particle size of the powders has been listed in Table 2 (SEM particle size). Higher temperature leads to larger particle size and better intergranular connectivity, revealing systematic grain growth.

Application of the Scherrer equation to the X-ray data leads to an estimated crystallite size of 15 nm (at 1100 °C). Although the value is smaller than the size observed by SEM, it confirms crystallites are in the nanometric range and that particle size, which might be formed by several crystallites, has the same trend as observed by SEM (see Table 2). This further implies that the powder has a high sinterability.

SEM pictures for $BaZr_xPr_{0.7-x}Gd_{0.3}O_{3-\delta}$ ($x = 0.1$, 0.3, 0.5 and 0.7) are displayed in Fig. 6. The powders calcined at 1100 °C (Fig. 6a) show, for all compositions, significant agglomeration, and the material presents a ''sheet-like'' morphology, whereas one may observe the presence of individual interconnected nanometric particles (about 100 nm) where those are visible (e.g. in Fig. 5b). The morphology at 1100 °C is very similar for all compositions. However, the microstructure of the powders is influenced by the Pr/Zr ratio, particularly observable for higher calcination temperatures; 1300 °C is shown as example in Fig. 6b. The main differences are found in the grain size, where Zr additions may retard the grain growth, and this might be also related to the different sintering activities of $BaZrO_3$ and $BaPrO_3$ materials. It has been reported that Gd:$BaPrO_3$ powders are highly sinterable (dense specimens can be obtained at 1400 °C using simple uniaxial pressing) [12], while for $BaZrO_3$-based materials is not possible to achieve dense material in equivalent conditions [27]. Studies based on similar a system showed that the sintering temperature increased depending on x for $BaCe_{0.9-x}Zr_xY_{0.1}O_{3-\delta}$, as reported by Katahira et al. [18]. The reason why Pr may accelerate grain growth (and probably final sintering of the specimens) in $BaZr_xPr_{0.7-x}Gd_{0.3}O_{3-\delta}$ is thought to relate to the relative refractory properties of the Pr and Zr oxides. As ZrO_2 is more refractory than PrO_x then it is more difficult to react/sinter.

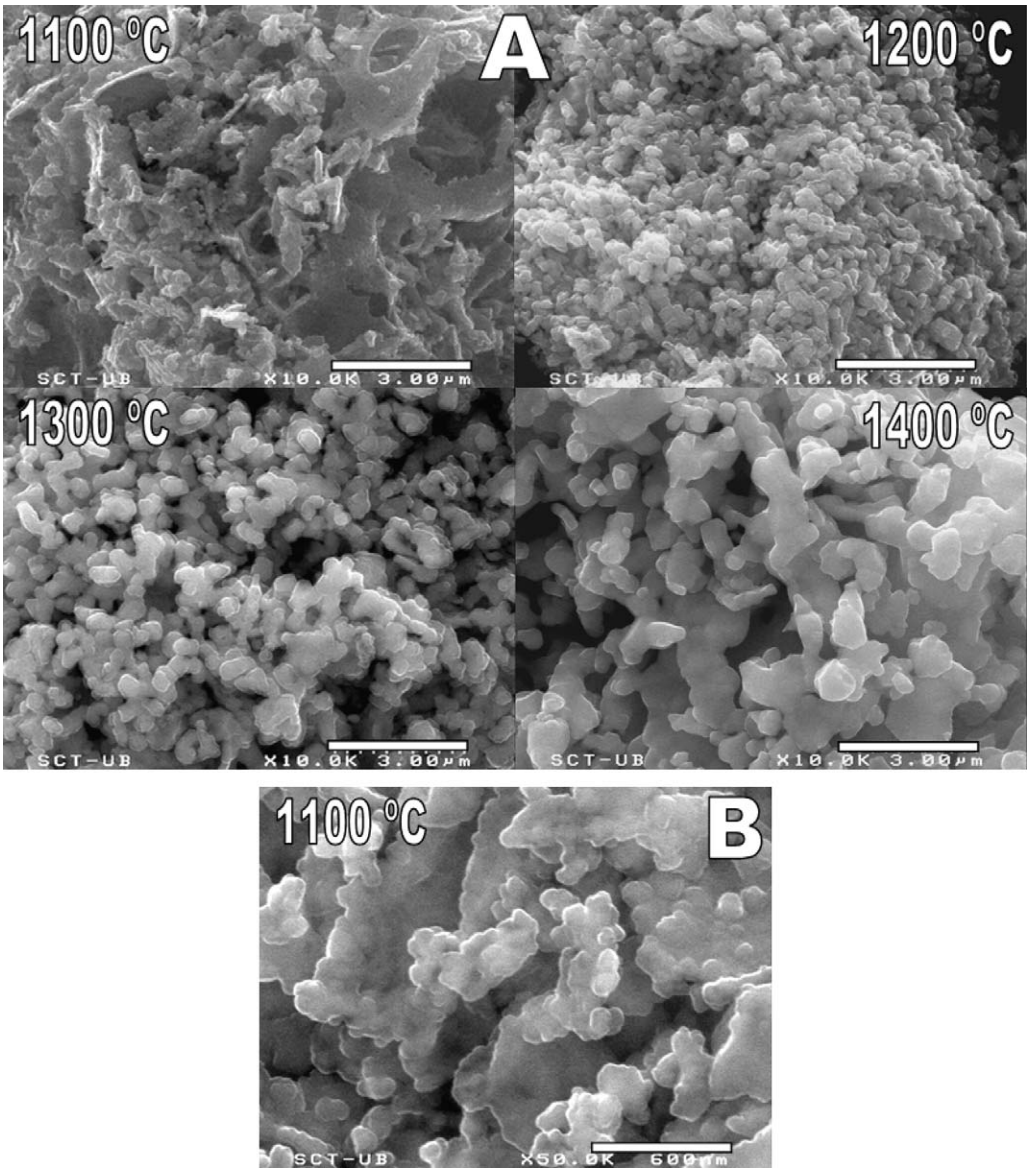

Fig. 5. (a) SEM micrographs of $BaZr_xPr_{0.7-x}Gd_{0.3}O_{3-\delta}$ ($x = 0.4$) calcined at 1100, 1200, 1300 and 1400 °C during 10 h and (b) higher magnification micrograph of the powder calcined at 1100 °C.

3.3. Thermal analysis

The TGA curves measured in CO_2 for all $BaZr_xPr_{0.7-x}Gd_{0.3}O_{3-\delta}$ samples are presented in Fig. 7. The materials containing little or no Zr, for example $BaPr_{0.7}Gd_{0.3}O_{3-\delta}$ and $BaZr_{0.1}Pr_{0.6}Gd_{0.3}O_{3-\delta}$ showed an appreciable weight gain starting at 300 °C, indicating that reaction with CO_2 had occurred as per the following equation:

$$BaPrO_3 + CO_2(g) \rightarrow BaCO_3 + PrO_2 \quad (1)$$

Further heating induced a weight loss at ca. 800 °C (for $x = 0$, 0.1), implying the reverse reaction had taken place, and CO_2 was released. During subsequent cooling after reaching 1000 °C, none of materials are reactive no more.

The maximum and total weight gain in the TGA curves diminishes gradually from $x = 0.2$ to $x = 0.7$ (Fig. 7). $BaPr_{0.7}Gd_{0.3}O_{3-\delta}$ has a maximum weight increase due to reaction with CO_2 of nearly 14%, while this is reduced below 2% for $BaZr_{0.5}Pr_{0.2}Gd_{0.3}O_{3-\delta}$. Also, the temperature for the beginning of the reactivity is retarded from 300 to 400 °C ($x = 0$) up to 500 to 600 °C ($x > 0.2$). XRD patterns collected after TG measurement under CO_2 clearly evidenced the presence of $BaCO_3$ and confirmed that reaction with CO_2 had

Table 2
Particle size and agglomerate size of the powder fired at different temperatures, by SEM compared to those estimated by Scherrer equation.

	Temperature (°C)			
	1100	1200	1300	1400
SEM particle size (nm)	80–120	200–300	200–400	400–600
SEM agglomerate size (μm)	0.25–1	0.5–1.5	1–2	1–4
Scherrer (nm)	15	30	55	–

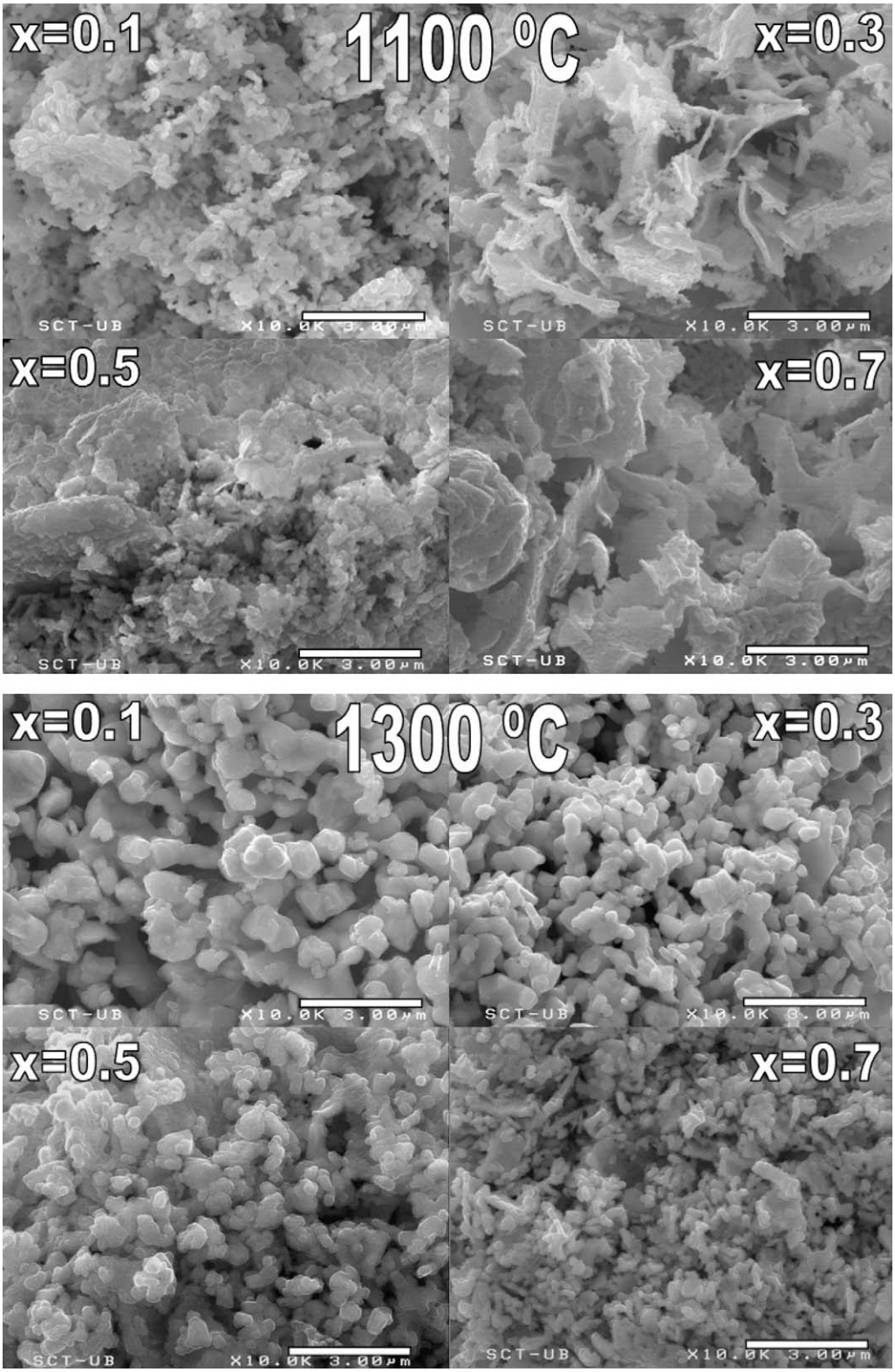

Fig. 6. SEM micrographs of the series $BaZr_xPr_{0.7-x}Gd_{0.3}O_{3-\delta}$ ($x = 0.1$, 0.3, 0.5 and 0.7) calcined at 1100 °C (a) and 1300 °C (b), for 10 h.

taken place for low Zr content materials, while showed essentially no $BaCO_3$ for $x > 0.5$.

The final weight uptake of $BaZr_xPr_{0.7-x}Gd_{0.3}O_{3-\delta}$ materials clearly diminished as a function of Zr-content. This result means that chemical stability of Zr-substituted $BaPrO_3$ against CO_2 increases with increasing Zr-content, as $BaPrO_3$ is very reactive towards CO_2 due to formation of $BaCO_3$, but $BaZrO_3$ is rather stable in CO_2. A previous report on thermogravimetric measurements under CO_2 of pure $BaPrO_3$ and $BaZrO_3$ also support this finding [9].

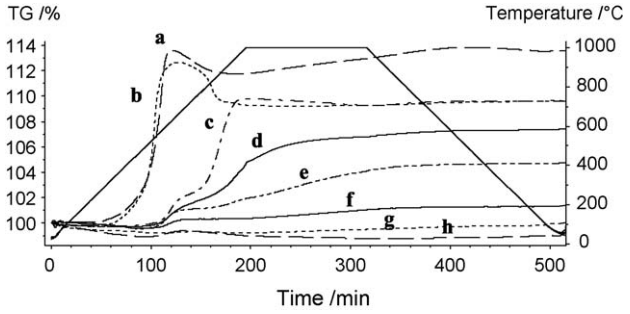

Fig. 7. TGA plot for $BaZr_xPr_{0.7-x}Gd_{0.3}O_{3-\delta}$ ($0 \geq x \geq 0.7$) samples run under 100% CO_2 at a rate of 5 °C/min. The letters a–h stand for $x = 0, 0.1, 0.2, 0.3, 0.4, 0.5, 0.6$ and 0.7, respectively.

The TGA curves for wet 5% H_2/Ar are somewhat more complex. Compositions with low Zr concentration showed a significant weight uptake between 450 and 650 °C that can be mainly ascribed to the reaction of decomposition of the perovskite, namely to form barium and praseodymium hydroxides, accompanied by the reduction of Pr(IV) to Pr(III) as described in more detail in Ref. [12]. For compositions with higher Zr content ($x \geq 0.5$), such weight gain did not occur.

The powders were characterized by XRD after the TG measurements (Fig. 8a), and $BaCO_3$ (pdf: 45-1471), $Pr(OH)_3$ (pdf: 83-2304), $Ba(OH)_2{\cdot}3H_2O$ (pdf: 21-0074) and $BaGd_2O_4$ (pdf: 19-0105)/$BaPr_2O_4$ (pdf: 48-0467), in addition to the perovskite phase, could be identified. The amount of decomposition products was found to consistently decrease as the ratio Zr/Pr increased, as expected by increased stability and the redox inactivity of $BaZrO_3$ compared to $BaPrO_3$. Consequently, the chemical reactions occurring under wet and/or reducing conditions can be ascribed to the reactivity of Pr, so we can understand the reactions involved here by writing the following equations:

$$2BaPrO_3 \rightarrow BaPr_2O_4 + (1/2)O_2(g) + BaO \quad (2)$$

$$BaPrO_3 + (5/2)H_2O(g) \rightarrow Pr(OH)_3 + Ba(OH)_2 + (1/2)O_2(g) \quad (3)$$

$$Ba(OH)_2 + CO_2 \rightarrow BaCO_3 + H_2O(g) \quad (4)$$

The use of 5% H_2/Ar acts, therefore, as a reducing gas for praseodymium from its oxidized state (IV) down to (III), and forms $BaPr_2O_4$ according to reaction (2), or $Pr(OH)_3$ with the presence of water, according to reaction (3). We may note that what we identified in the XRD patterns is a solid solution of $BaGd_2O_4$ and $BaPr_2O_4$, so that part of the Gd(III) acting as a dopant in $BaZr_xPr_{0.7-x}Gd_{0.3}O_{3-\delta}$ is also involved into this new reduced material, $BaPr_2O_4$, and consequently wrote is as $Ba(Pr,Gd)_2O_4$.

Water has a reducing effect in $BaPrO_3$, and hydrates both Ba(II) and Pr(IV) to $Ba(OH)_2$ and $Pr(OH)_3$, as per Eq. (3). However, it is sometimes difficult to find barium hydroxide in our X-ray patterns, since it rapidly transforms into $BaCO_3$ (Eq. (4)), which is easily found in our XRD patterns.

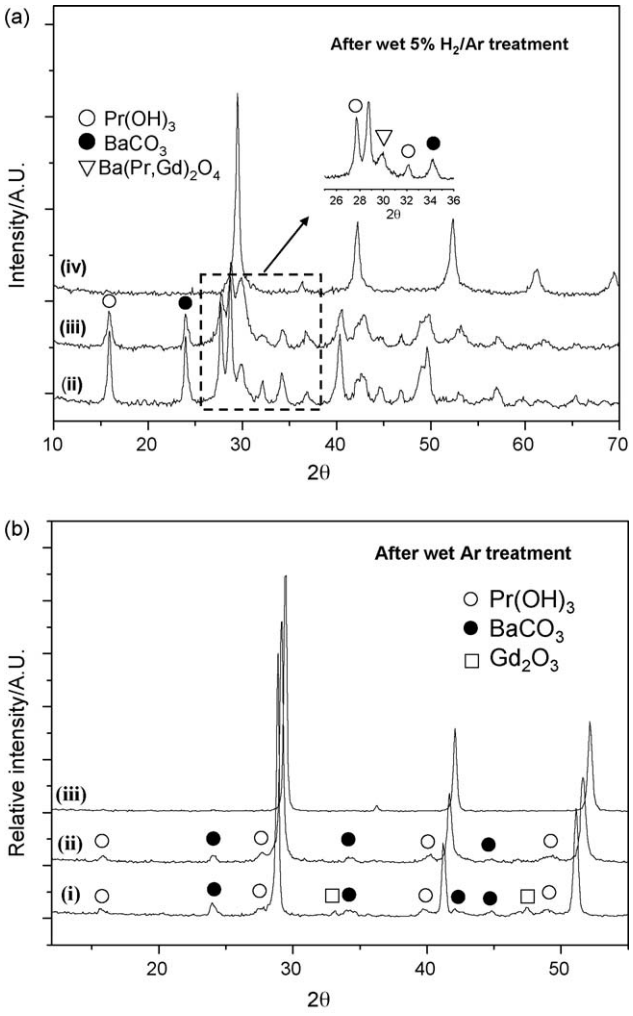

Fig. 8. X-ray diffraction patterns for $BaZr_xPr_{0.7-x}Gd_{0.3}O_{3-\delta}$ after the thermal treatment in: (a) wet 5% H_2/Ar and (b) wet Ar (final temperature = 900 °C). (i)–(iv) denote $x = 0$, 0.2, 0.4 and 0.5, respectively. Unmarked peak in the inset corresponds to the perovskite phase.

As displayed in Fig. 8a, $BaZr_xPr_{0.7-x}Gd_{0.3}O_{3-\delta}$ decomposes in wet 5% H_2/Ar mixture for $x < 0.4$, while the pattern for $x = 0.5$ looks unaltered. In fact, we could observe that the higher the Zr content, the lower the total weight uptake in the TG curves of the perovskite was, indicating less degree of decomposition into the hydroxide phases. We can then conclude that there is a good stabilization of the material when $x \geq 0.5$ under wet reducing conditions.

A similar result is encountered for the TGA under wet Ar. X-ray diffraction performed after the analysis (Fig. 8b) confirms that the compositions $x \geq 0.4$ for $BaZr_xPr_{0.7-x}Gd_{0.3}O_{3-\delta}$ do not decompose with water containing atmospheres in the studied range of temperature, and they are thus stable. The chemical reactions occurring under wet Ar can be described as per Eq. (3). In addition to $BaCO_3$ and $Pr(OH)_3$, also Gd_2O_3 (pdf: 12-0797) was encountered. However, we may note here that the reactivity in wet Ar is much less severe than under reducing conditions, indicating, thus, that Pr(IV) is easily reduced to Pr(III) and easily decomposed.

This study demonstrates quite clearly that introduction of $BaZrO_3$ into Gd-doped $BaPrO_3$ greatly enhances the chemical stability. We can then conclude that the scope of this work, i.e. stabilizing Gd:$BaPrO_3$ by Zr-substitution, has been achieved for a Zr content over 0.4–0.5.

The high dopant levels of Gd(III) were chosen in the present study so as to favour the formation of oxygen vacancies in the dry state, which are, in turn, in equilibrium with the surrounding atmosphere to form, for instance, electron holes or protons [28], and these defects can give rise to enhanced oxide ion, protonic or p-type conductivity: an important goal for an SOFC material. Unfortunately, microstructural investigations show that the perovskite becomes unstable, as Gd_2O_3 segregation (pdf: 42-1465) occurs when a high temperature (and long) thermal treatment is applied. The XRD pattern evolution for $BaZr_{0.6}Pr_{0.1}Gd_{0.3}O_{3-\delta}$ after this more severe thermal treatment (temperatures typically around 1500 °C, for more than 30 h) is shown as example in Fig. 9. This was further verified by SEM (Fig. 10) on samples sintered at 1500 °C during 30–35 h. The presence of a whiter phase seen in the BSE image was analyzed by EDS microanalysis, and found it was Gd-rich, which clearly shows the segregation effect. This phenomenon happens for all compositions in the $BaZr_xPr_{0.7-x}Gd_{0.3}O_{3-\delta}$ family, indicating that introducing 30% of Gd in the perovskite structure, a high dopant concentration, is not stable. It can be suggested that long-term annealing leads to a small compositional change (e.g. BaO loss) that moves the composition to outwith the domain of single phase solid solution behaviour causing Gd_2O_3 exsolution. By way of contrast, early investigations on less heavily doped materials ($BaZr_xPr_{0.9-x}Gd_{0.1}O_{3-\delta}$) show no evidence of such happening. Further research on these materials is currently underway.

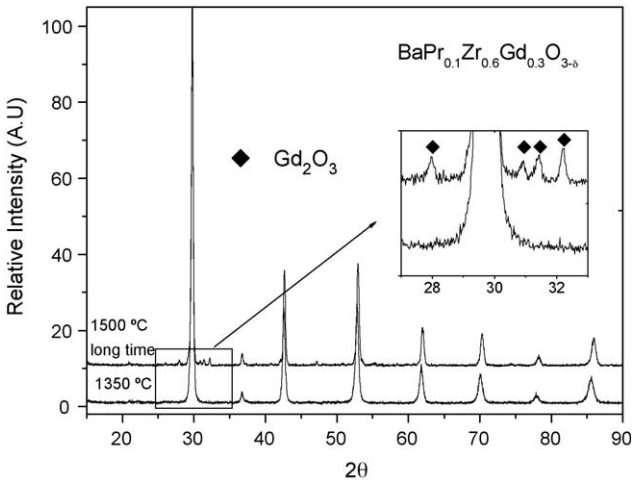

Fig. 9. XRD patterns for $BaZr_xPr_{0.7-x}Gd_{0.3}O_{3-\delta}$ ($x = 0.6$) demonstrating Gd_2O_3 segregation occurring after long thermal treatment at 1500 °C.

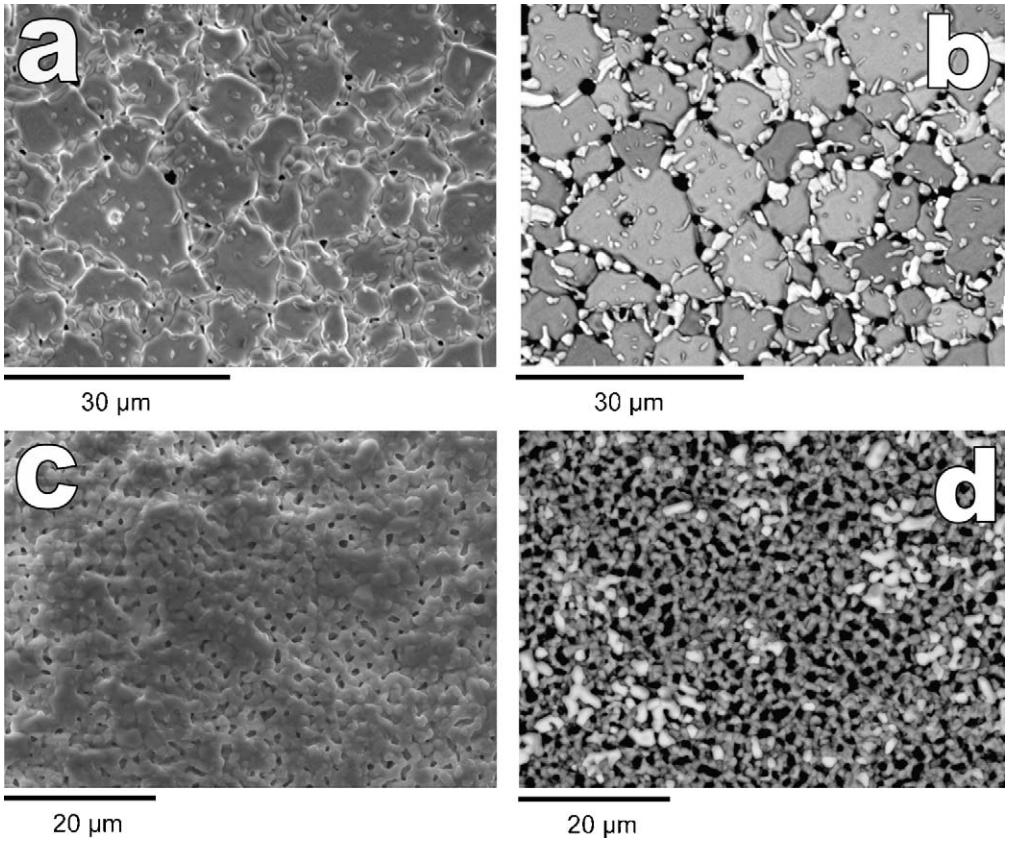

Fig. 10. SEM micrographs using both the secondary (left side) and backscattered electrons (right side) imaging to demonstrate Gd-rich phase segregation in: $BaZr_xPr_{0.7-x}Gd_{0.3}O_{3-\delta}$ (a and b) $x = 0$ and (c and d) $x = 0.6$. The whiter precipitates in the BSE image is a Gd-rich phase (by EDS).

4. Conclusions

A large extent of mutual solubility between $BaPrO_3$–$BaZrO_3$ has been demonstrated in the quasi binary system doped with Gd at a fixed concentration (30%) using the acrylamide combustion synthesis. It is also found that $BaZrO_3$ is an excellent additive for stabilizing the Gd-doped $BaPrO_3$ perovskite. $BaZr_xPr_{0.7-x}Gd_{0.3}O_{3-\delta}$ ($x = 0$–0.3) are unstable in wet Ar and/or wet 5% H_2/Ar and decompose to form hydroxides and/or reduced species; $BaZr_{0.4}Pr_{0.3}Gd_{0.3}O_{3-\delta}$ is stable under wet Ar, but still sensitive to reduction in wet 5% H_2/Ar, while $BaZr_xPr_{0.7-x}Gd_{0.3}O_{3-\delta}$ ($x \geq 0.5$) proved to be stable under all conditions. Given the redox inactivity of $BaZrO_3$ and higher chemical stability compared to $BaPrO_3$, the reactivity towards CO_2, water and reducing atmospheres greatly diminishes with increasing Zr content ($x > 0.4$). The nanoparticulate materials were in the range between 80 and 120 nm, explored by SEM. Powder X-ray diffraction reveals that $BaZr_xPr_{0.7-x}Gd_{0.3}O_{3-\delta}$ materials were all cubic (or nearly cubic) single phase perovskites. Unfortunately, the materials suffer from gadolinium segregation under more severe thermal treatments, therefore, reducing the trivalent dopant content, i.e. $BaZr_xPr_{0.9-x}Gd_{0.1}O_{3-\delta}$, is suggested.

Acknowledgements

We would like to thank Prof. Cuevas (Dep. Geology, UB) for experimental data, Pep Bassas for X-ray sample preparation and SEM facilities at the Scientific and Technical Services (UB, Barcelona). Also, CeRMAE (Generalitat de Catalunya) and EPRSC for funding.

References

[1] T. Norby, Solid State Ionics 125 (1999) 1–11.
[2] K. Kreuer, Chem. Mater. 8 (1996) 610–641.
[3] H. Iwahara, Solid State Ionics 77 (1995) 289–298.
[4] T. Schober, Solid State Ionics 162–163 (2003) 277–281.
[5] H. Iwahara, H. Uchida, K. Ono, K. Ogaki, J. Electrochem. Soc. 135 (1988) 529–533.
[6] N. Bonanos, Solid State Ionics 53–56 (1992) 967–974.
[7] H. Iwahara, Y. Asakura, K. Katahira, M. Tanaka, Solid State Ionics 168 (2004) 299–310.
[8] T. Fukui, S. Ohara, S. Kawatsu, J. Power Sources 71 (1998) 164–168.
[9] L. Li, J.R. Wu, S.M. Haile, Electrochem. Soc. Proc. 12 (2001) 214–223.
[10] S. Mimuro, S. Shibako, Y. Oyama, K. Kobayashi, T. Higuchi, S. Shin, S. Yamaguchi, Solid State Ionics 178 (2007) 641–647.
[11] V.P. Gorelov, B.L. Kuzin, V.B. Balakireva, N.V. Sharova, G.K. Vdovin, S.M. Beresnev, Russ. J. Electrochem. 37 (5) (2001) 505–511.
[12] A. Magrasó, F. Espiell, M. Segarra, J.T.S. Irvine, J. Power Sources 169 (2007) 53–58.
[13] K.A. Furøy, R. Haugsrud, M. Hänsel, A. Magrasó, T. Norby, Solid State Ionics 178 (2007) 461–657.
[14] F.L. Chen, O.T. Sorensen, G.Y. Meng, D.K. Peng, J. Mater. Chem. 7 (1997) 481.
[15] K.D. Kreuer, Annu. Rev. Res. 33 (2003) 333–359.
[16] M.J. Scholten, J. Schoonman, J.C. Van Miltenburg, H.A.J. Oonk, Solid State Ionics 61 (1993) 83.
[17] S.V. Bhide, A.V. Virkar, J. Electrochem. Soc. 146 (12) (1999) 4386–4392.
[18] K.H. Ryu, S.M. Haile, Solid State Ionics 125 (1999) 355.
[19] K. Katahira, Y. Kohchi, T. Shimura, H. Iwahara, Solid State Ionics 138 (2000) 91.
[20] A. Tarancón, G. Dezanneau, J. Arbiol, F. Peiró, J.R. Morante, J. Power Sources 118 (2003) 256–264.
[21] A. Sin, P. Odier, Adv. Mater. 12 (9) (2000) 649–652.
[22] A. Magrasó, A. Calleja, X.G. Capdevila, F. Espiell, Solid State Ionics 166 (3–4) (2004) 359–364.
[23] J. Rodríguez-Carvajal, M.T. Fernandez-Díaz, J.L. Martínez, J. Phys. Condens. Matter 3 (1991) 3215.
[24] A.J. Jacobson, B.C. Tofield, B.E.F. Fender, Acta Crystallogr. Sec. B 28 (1972) 956.
[25] H.E. Swanson, N.Y. Gilfrich, G.M. Ugrinic, Standard X-Ray Powder Diffraction Patterns Vol. 5, Natl. Bur. Std. (U.S.) Circ., 539 (1955) 75.
[26] R.D. Shannon, Acta Cryst. A32 (1976) 751.
[27] Z. Zhong, Solid State Ionics 178 (2007) 213–220.
[28] A. Magrasó, R. Haugsrud, M. Segarra, T. Norby, J. Electroceram. (2008), doi:10.1007/s10832-008-9541-z.